MRI-powered Actuators for Robotic Interventions

Panagiotis Vartholomeos[Member, IEEE],
Cardiac Surgery, Children's Hospital Boston, Harvard Medical School, Boston, MA 02115 USA

Lei Qin, and
Radiology, Brigham and Women's Hospital, Harvard Medical School, Boston, MA, 02115 USA

Pierre E. Dupont[Fellow, IEEE]
Cardiac Surgery, Children's Hospital Boston, Harvard Medical School, Boston, MA 02115 USA

Panagiotis Vartholomeos: panagiotis.vartholomeos@childrens.harvard.edu; Lei Qin: leiqin@bwh.harvard.edu; Pierre E. Dupont: pierre.dupont@childrens.harvard.edu

Abstract

This paper presents a novel actuation technology for robotically assisted MRI-guided interventional procedures. Compact and wireless, the actuators are both powered and controlled by the MRI scanner. The design concept and performance limits are described and derived analytically. Simulation and experiments in a clinical MR scanner are used to validate the analysis and to demonstrate the capability of the approach for needle biopsies. The concepts of actuator locking mechanisms and multi-axis control are also introduced.

I. Introduction

The importance of robotically-assisted MR-guided interventions is well recognized by the clinical and research communities [1]. In these procedures, the robot provides precision, accuracy, speed and also offers the possibility for remote operation. The high quality images and the well-defined 3D coordinate system provided by MRI facilitate periodic updates to the planned trajectory of the robotic interventional tool and enable compensation for intraoperative organ and tissue deformations [2].

The development of MRI interventional robotic systems face several challenges related to compatibility and space constraints. The actuators must ensure MRI safety, preserve image quality, and be able to operate unaffected by the scanner's electric and magnetic fields distortion [1]. Several groups worldwide have developed MR-compatible robotic systems [3–9]. These systems are usually specific to the prostate, breast or brain, and most perform the task of needle guidance for biopsies or interventional therapies.

Conventional actuation principles involving electromagnetic actuators are generally not MR-compatible. Therefore alternative actuation principles are employed, such as ultrasonic motors and pneumatic actuators. For example, the MR-compatible robots of [3–5] for needle-based interventions all employ ultrasonic motors. MR compatibility measurements demonstrated that when ultrasonic motors are placed inside the MRI bore and are powered on, there is large reduction in imaging SNR [6]. Consequently, actuation and imaging must be interleaved; making the implementation of real-time control more difficult [1]. Ultrasonic motors can be continuously operated only if they are placed at a distance from the bore, but flexibility, backlash and friction are introduced due to remote actuation of joints [5].

Pneumatic actuators, in contrast, do not cause SNR reduction, but they do require a complicated installation that involves locating a control unit, power supplies, amplifiers and valves externally to the MRI shielded room [7,8]. Furthermore, the pneumatic transmission

lines lower the bandwidth and, in combination with the spatial constraints of the MRI bore, complicate robot design [9].

The contribution of this paper is to propose an actuator technology that is both powered and controlled by the MRI scanner. The principle of operation is based on one or more small ferromagnetic bodies embedded in the actuator that serve to convert the electromagnetic energy of the MR gradients into mechanical energy. The ferromagnetic bodies have a small volume and can be designed to be outside the imaging region of interest. Thus, they do not affect imaging quality. The actuators themselves are also wireless and compact. In addition, since the MR system provides both imaging and control of the interventional procedure using a common software interface, the integration of actuation and imaging is simplified.

The use of MRI gradients to induce motion to ferromagnetic particles in the vasculature has been previously performed [10,11,12]. For example, Martel et al. demonstrated closed-loop trajectory control of a 1.5 mm diameter ferromagnetic sphere in the carotid artery of a pig [10,11]. In these papers, the ferromagnetic particle is the robot. This work inspired us to think of ways to use the same force production principles to design actuators that could power more general interventional robots. The result is the actuator technology described here.

The remainder of the paper is organized as follows: Section II reviews the background theory on the generation of actuator forces by the MRI scanner. Section III describes the design of a prototypical actuator. Actuator dynamics are presented in Section IV and open-loop stability is also analyzed. Section V presents validation experiments performed in a clinical MRI. These experiments demonstrate the force production capabilities of the actuator. They also demonstrate the concept of an actuator locking mechanism to avoid accidental actuator motion as well as to enable independent control of multiple actuators. Conclusions appear in the final section of the paper.

II. Background Theory

When a ferromagnetic body is placed inside an MRI bore, it becomes magnetized due to the strong and uniform B_0 central field directed along the axis of symmetry of the bore. The magnetization across the volume of the body can be approximated as a lumped effect at the center of mass (CM) of the body [13]. Consequently, the magnetized body is approximated by a magnetic dipole placed at its CM. For typical central field strengths, the magnetization magnitude asymptotically approaches the saturation magnetization value $\vec{M}_s$ of the material, and its direction points along the easy magnetization axis of the body, which depends on the shape anisotropy of the material. The magnetic torque and force acting on the body can be computed using the expressions for the torque $\vec{T}$ and force $\vec{F}$ acting on a magnetic dipole in an external field $\vec{B} = \vec{B}_0 + \vec{B}_g$:

$$\vec{T} = V\vec{M}_s \times \vec{B} \tag{1a}$$

$$\vec{F} = nV(\vec{M}_s \cdot \nabla)\vec{B} \tag{1b}$$

where $\vec{B}_g$ is the magnetic field generated by the gradient coils, V is the magnetic volume of the material, $\vec{M}_s$ is the saturated magnetization per unit volume of the material, and n is the duty cycle fraction of the MRI gradients. The magnetic torque $\vec{T}$ tends to rotate the ferromagnetic body so that the magnetization vector $\vec{M}_s$ aligns with the direction of the

external B_0 field (the contribution of the B_g field to the torque $\vec{T}$ is negligible). Since the B_0 field inside an MRI is fixed and cannot be controlled by the user, the torque $\vec{T}$ is not a valuable quantity for control purposes.

The magnetic forces $\vec{F}$ depend on the spatial variation of the field $\vec{B}_g$, generated by the gradient coils. These comprise a pair of Maxwell coils and four pairs of saddle coils located orthogonal to each other as shown in Fig. 1, [14].

Resolving the force $\vec{F}$ of (1b) in the XYZ frame that is attached to the isocenter of the bore (see Fig. 1), yields:

$$\begin{bmatrix} F_x & F_y & F_z \end{bmatrix}^T = nVM_{sz} \begin{bmatrix} \frac{\partial B_{gx}}{\partial z} & \frac{\partial B_{gy}}{\partial z} & \frac{\partial B_{gz}}{\partial z} \end{bmatrix}^T \tag{2}$$

where it has been reasonably assumed that $M_{sx}, M_{sy} \ll M_{sz}$. Equation (2) shows that the MRI forces acting on a ferromagnetic body are related to the three gradients of (2). The gradient coils are designed to generate (for imaging purposes) the three linearly independent gradients of (3).

$$\vec{g} = \begin{bmatrix} g_x & g_y & g_z \end{bmatrix}^T = \begin{bmatrix} \frac{\partial B_{gz}}{\partial x} & \frac{\partial B_{gz}}{\partial y} & \frac{\partial B_{gz}}{\partial z} \end{bmatrix}^T \tag{3}$$

The Maxwell equations state that field lines must form closed loops, however, i.e. $\nabla \cdot B = 0$, and also that they must exhibit zero curl, i.e. $\nabla \times B = 0$, at any point outside the coil conductors. This implies that it is impossible to generate the gradients in (3) without also generating concomitant gradients. As a result, the complete field B_g is given by [15]:

$$\vec{B}_g(\vec{x}) = (\vec{g} \cdot \vec{x})\hat{z} + \mathbf{G}_c \vec{x} \tag{4}$$

where $\vec{g}$ is as given in (3), $\vec{x}$ is the position vector from the origin of the XYZ frame, $\hat{z}$ is the unit vector along the z-axis and $\mathbf{G}_c$ is a matrix containing the concomitant gradients and is given by:

$$\mathbf{G_c} = \begin{bmatrix} -g_z/2 & 0 & g_z \\ 0 & -g_z/2 & g_y \\ 0 & 0 & 0 \end{bmatrix} \tag{5}$$

Differentiating the x and y components of (4) with respect to the z coordinate yields:

$$\frac{\partial B_{gx}}{\partial z} = \frac{\partial B_{gz}}{\partial x}, \frac{\partial B_{gy}}{\partial z} = \frac{\partial B_{gz}}{\partial y} \tag{6}$$

Hence, the gradients of (2) are equal to the imaging gradients of (3) and, furthermore, all three are linearly independent. Thus, they are capable of inducing 3 degree of freedom (DOF) motion in a ferromagnetic body.

III. Actuator design

The proposed actuator is comparable to an electric motor. It consists of the stator, which, in this case, is comprised of the MRI scanner together with the stationary components of the actuator, and a rotor, which is the rotating portion of the actuator that contains the ferromagnetic material. As depicted in Fig. 2, the rotor consists of a ferromagnetic object enclosed in a cavity in a lever arm that rotates at a fixed distance about an axis. The cavity must be located at the maximum possible moment arm to provide maximum torque.

The object is contained in a cavity rather than embedded in the lever arm since, by (1a), a large torque would be generated if rotation of the lever arm caused the magnetization vector of the sphere to rotate out of alignment with the B_0 field. Except in the case that the actuator axis was perfectly aligned with the central axis, such a torque would stall the actuator. Therefore, the ferromagnetic body must be free to rotate within its cavity. To minimize friction between the ferromagnetic body and the cavity walls, the geometry of the ferromagnetic body should be selected as spherical and the surfaces of the sphere and cavity should be designed to minimize friction.

All actuator components are nonferrous apart from the embedded ferromagnetic body. The preferred ferromagnetic material is chrome steel because it has the second highest saturation magnetization among the ferromagnetic materials ($\sim 1.4 \cdot 10^6 \, Am^{-1}$), it can very easily be machined into spherical shape and its surface has very low roughness [16].

Rotation of the actuator is generated by applying magnetic field gradients to generate a force $\vec{F}$ on the ferromagnetic sphere as shown in Fig. 2. Assuming for simplicity that the *xyz* frame of the actuator coincides with the *XYZ* frame of the isocenter of the MRI bore (Fig. 1), gravity is directed along the *y* axis and so does not affect rotor motion.

From the free-body diagram of Fig. 3, the single degree of freedom motion is described by the following scalar equation

$$J\ddot{\theta} = -b\,\dot{\theta} + r_1 F \sin(\varphi - \theta) \tag{7}$$

in which J is the moment of inertia of the composite body that comprises the axis, the lever and the sphere, r_1 is as shown in Fig. 3, b is the coefficient of viscous friction, and θ is the angle of the rotor, and φ is the angle of the magnetic gradient.

The angle θ is called the *mechanical angle*, and the angle φ is called the *magnetic angle*. Their difference is called the *slip angle, s*:

$$s = \varphi - \theta \tag{8}$$

and is a critical parameter for the analysis of the motor. F and φ are given by:

$$F = \left\| \vec{F} \right\| = \sqrt{F_x^2 + F_z^2}, \varphi = \tan^{-1}(F_x/F_z) \tag{9}$$

where F_x, F_z are as given in Eq. (2).

The maximum allowable gradient of a clinical MRI is 40 mT/m, which results in a small magnetic force $\vec{F}$ (on the order of tens of mN for magnetic volumes of a few mm^3). This

limitation can be addressed using transmission elements to provide interventional-level forces. Candidate solutions include gear trains, screws and harmonic drives.

The experimental actuator presented later in the paper employs gears together with a rack and pinion to produce linear motion, as illustrated schematically in Fig. 4. The pinion N_1 is keyed to the lever and transmits the lever motion to the rest of the transmission elements, which consist of three gears, three pinions, and one rack. All rotations as well as the rack translation take place on the x–z plane.

The reduction ratio between θ and the rack speed u_r is:

$$R = \frac{u_r}{\dot\theta} = \frac{r_2}{G_1 G_2 G_3}$$

(10)

The G_1, G_2, G_3 are transmission ratios given by:

$$G_1 = N_2/N_1, G_2 = N_4/N_3, G_3 = N_6/N_5$$

(11)

while N_i, $\{i = 1,..,6\}$ are the gear teeth, and r_2 is the radius of the N_7 pinion.

To maximize output force, the x–y plane of the rotor has to coincide with the X–Z plane of the MRI bore. Otherwise, part of the magnetic force is used for compensating gravity. If the output force has to be applied at an angle with respect to the x–y plane, then bevel gears can be used to change the axis of rotation.

IV. Dynamic Model and Stability Analysis

The performance characteristics of the proposed actuator technology can be determined from an analysis of the governing dynamic equations. The analysis focuses on the rotor characteristics, since the stator, i.e. the MRI scanner, cannot be modified. To this end, (9) is extended to incorporate the transmission as well as terms for non-viscous friction and load:

$$J\frac{d\dot\theta}{dt} = -B\dot\theta - T_{fr} - RF_l + r_1 F\sin(\varphi - \theta)$$

(12a)

$$u_r = R\dot\theta$$

(12b)

Here, R and u_r are defined in (10). The terms J and B are the summation of the inertia and viscous friction terms, respectively, of all transmission stages as seen by the input of the system. The term T_{fr} is the summation of all non-viscous friction terms as seen by the input including the friction component contributed by the ferromagnetic sphere when it slides inside the cavity. The non-viscous friction terms are modeled as constants and F_l is the load applied on the tip of the rack. It is reasonably assumed that the eddy currents induced on the millimeter-scale chrome steel sphere are very small and can be neglected [17].

A. Actuator performance with closed-loop control of slip angle

Closed-loop actuator control requires using the MRI scanner to both measure the actuator state and to apply the actuation force. While this approach does require sophisticated and

nonstandard MRI programming, it has been previously demonstrated for the navigation of spherical particles in the vasculature [11].

In a typical robotic intervention, the robot's actuators would be operated in a position or velocity control loop so as to drive the tool, e.g., biopsy needle, to a desired location. In such an application, an inner control loop can be implemented for each actuator that regulates its slip angle to $s = \pi/2$ so as to maximize the force or torque that can be generated by the actuator. The steady-state output linear velocity u_r is given by:

$$
\begin{aligned}
u_r &= -\frac{R^2}{Br_2}F_l + R\left(\frac{r_1 F}{B} - \frac{T_{fr}}{B}\right) \\
&= -\frac{R^2}{Br_2}F_l + R\left(\frac{r_1 V M_s B_{grad}}{B} - \frac{T_{fr}}{B}\right)
\end{aligned}
\tag{13}
$$

where

$$
B_{grad} = \left((\partial B_{gx}/\partial z)^2 + (\partial B_{gy}/\partial z)^2\right)^{1/2}
\tag{14}
$$

is constant. Eq. (13) reveals that when the slip angle is regulated at a constant value, then the output velocity u_r is linearly related to the output force F_l through a negative proportionality constant.

The maximum permissible output load (stall or blocking force) is obtained for $u_r = 0\ ms^{-1}$ and is given by:

$$
F_{l\_max} = (r_1 V M_s B_{grad} - T_{fr})/R
\tag{15}
$$

The mechanism is not able to generate output forces greater than F_{l_max}. Setting the output force F_l to zero yields the maximum output velocity u_{r_max}. This maximum output velocity corresponds to a maximum rotational velocity of the lever $\theta_{max} = u_{r\_max}/R$, which in turn gives the maximum gradient frequency ω_{max} for a given B_{grad}:

$$
\omega_{max} = \frac{r_1 V M_s B_{grad}}{B} - \frac{T_{fr}}{B}
\tag{16}
$$

The mechanism is not able to respond to a gradient rotating at frequencies greater than ω_{max}.

B. Actuator performance without control of slip angle

The preceding subsection proposed a nested control structure in which an inner control loop regulates slip angle and an outer loop controls actuator position or velocity. This subsection addresses the simpler case in which slip angle is not controlled. To understand if this approach may suffice for simple interventional applications, this subsection studies the stability of two important cases. The first is when a constant load is applied to the actuator and it is driven at constant velocity. The second case corresponds to a linear elastic load driven at constant velocity. This latter case is comparable to the loading experienced by a biopsy needle pressing against tissue prior to puncture.

1) Constant-velocity constant-load stability—In this case, the MRI scanner is programmed to generate gradients rotating in the *X–Z* plane at constant frequency ω. The gradients are given by:

$$\left[\begin{array}{cc} \frac{\partial B_{gx}}{\partial z} & \frac{\partial B_{gz}}{\partial z} \end{array}\right]^T = B_{grad}\left[\begin{array}{cc} \cos\omega t & \sin\omega t \end{array}\right]^T \tag{17}$$

In the open loop case, stable operation of the actuator implies the rotor synchronizes with the rotating gradient frequency. To analyze the steady-state behavior of the system in response to the gradients of (17), (12a) is rewritten in state-space form as

$$\begin{array}{c} \dot{x}_1 = x_2 \\ \dot{x}_2 = -(B/J)x_2 - T_{fr}/J - RF_l/J + (r_1F/J)\sin(\omega t - x_1) \\ s = -x_1 + u \end{array} \tag{18}$$

where the slip angle s is considered a system output and is a linear function of the state x_1 and the input $u = \omega t$. The equilibrium point is found by setting $\dot{x}_1 = \omega$, $\dot{x}_2 = 0$, and is

$$x_1^* = \omega t - s^* \tag{19a}$$

$$x_2^* = \omega \tag{19b}$$

$$s^* = \sin^{-1}((B\omega + T_{fr} + RF_l)/(r_1F)) \tag{19c}$$

where s^* is the equilibrium slip angle. The stability of the system of (18) in the vicinity of the equilibrium point is determined via linearization with respect to the (x_1^*, x_2^*) point. To this end, the system of (18) is rewritten as:

$$\begin{array}{c} \dot{e}_1 = e_2 \\ \dot{e}_2 = -\frac{B}{J}e_2 + (\frac{B\omega + T_{fr} + RF_l}{J} - \frac{r_1F}{J}\sin(e_1 + s)) \end{array} \tag{20}$$

where

$$\left[\begin{array}{c} e_1 \\ e_2 \end{array}\right] = \left[\begin{array}{c} x_1^* - x_1 \\ x_2^* - x_2 \end{array}\right] \tag{21}$$

The linearization is evaluated at:

$$\mathbf{e} = \left[\begin{array}{cc} e_1 & e_2 \end{array}\right]^T = \left[\begin{array}{cc} 0 & 0 \end{array}\right]^T \tag{22}$$

and the linear state equations in vector form are given by $\dot{\mathbf{e}} = \mathbf{Ae}$, where $\mathbf{A}$ is the system matrix:

$$\mathbf{A} = \begin{bmatrix} 0 & 1 \\ -(Fr_1/J)\cos s^* & -B/J \end{bmatrix} \tag{23}$$

Stability analysis of $\mathbf{A}$ shows that the equilibrium point $\mathbf{e}^* = \begin{bmatrix} 0 & 0 \end{bmatrix}^T$ is: (1) a stable focus for $|s^*| < \pi/2$, (2) a saddle point for $s^* = \{-\pi/2, \pi/2\}$ and (3) an unstable focus for $|s^*| > \pi/2$.

Referring back to Fig. 3, what this analysis shows is that mechanical angle lags magnetic angle. By (19c), the amount of lag, s^*, increases monotonically from zero as a function of gradient frequency ω, static friction T_{fr} and load F_l. Since stability requires that $|s^*| < \pi/2$, and magnetic torque is maximized at $|s| = \pi/2$, constant-velocity constant-load performance is reduced compared to the case where the slip angle s is controlled.

2) Constant-velocity elastic-load stability—In biopsy applications, large forces are typically required to puncture tissue layers, however, the load applied to the needle prior to puncture is not constant, but rather is viscoelastic. As an approximation to the viscoelastic tissue deformation force prior to puncture, this subsection considers the effect of an elastic load on the stability of the actuator during constant velocity operation.

In this case, the MRI gradients are as given in (17). The actuator rotor synchronizes with the constant gradient frequency and the rack pushes at a constant speed against the elastic material. The load force is given by:

$$F_l = kl \Rightarrow F_l = kR\theta \tag{24}$$

where k is the tissue stiffness constant, and l is the deformation of the elastic load. Equation (18) is rewritten as:

$$\dot{x}_1 = x_2$$
$$\dot{x}_2 = -(Bx_2 + T_{fr} + kR^2 x_1)/J + (r_1 F/J)\sin(\omega t - x_1) \tag{25}$$

For this case, the equilibrium is given by

$$x_1^* = \omega t - s^* \tag{26a}$$

$$x_2^* = \omega \tag{26b}$$

$$s^* = \sin^{-1}\left((T_{fr} + B\omega)/(r_1 F) + k(R^2 \omega t)/(r_1 F)\right) \tag{26c}$$

Repeating the stability analysis of Eqs. (20–23) now yields the system matrix $\mathbf{A}$ as:

$$\mathbf{A} = \begin{bmatrix} 0 & 1 \\ -(kR^2 + Fr_1 \cos s^*)/J & -B/J \end{bmatrix} \tag{27}$$

The term kR^2 is three to five orders of magnitude smaller than Fr_1 and can be neglected. Consequently, e^* is again: (1) a stable focus for $|s^*| < \pi/2$, (2) a saddle point for, $s^* = \{-\pi/2, \pi/2\}$ and (3) an unstable focus for $|s^*| > \pi/2$.

Simulation was performed to examine how the steady-state speed of the mechanism, the output force, and the slip angle vary for increasing load. In this section only qualitative results are of interest, therefore gross estimates of the parameter values were used for the simulations. Example plots appear in Fig. 5. As shown, for approximately 20 seconds, the velocity remains constant as the elastic load deforms. At the same time, the increase in elastic deformation is compensated by a proportional increase in the slip angle (i.e. increase of the input magnetic force F).

This steady-state operation is maintained until the slip angle approaches $\pi/2$, at which point the actuator becomes unstable and begins to oscillate about a fixed position and zero velocity. Although the rotary oscillations of the lever are large, the transmitted oscillations to the output stage (the rack) are attenuated by the transmission ratio and so the output force exhibits small-amplitude oscillations about the value of the blocking force.

The blocking force is the maximum force that can be applied by the actuator on a load and is equal to F_{l_max} derived in the case of the controlled slip angle. Hence, when the actuator is pushing against an elastic material it can exert the stall force F_{l_max} even without controlling the slip angle, albeit with small oscillations.

V. Actuator Characterization Experiments

An actuator prototype was constructed using Lego components as shown in Fig. 6. Lego components offer a fast, easy and reliable way to build mechanisms that are MRI compatible. All components are plastic except for the bevel-type 21-gauge needle, which is made of (non-ferromagnetic) aluminum and the (ferromagnetic) chrome steel sphere. The dimensions of this prototype are 10×6×6 cm.

The experiments were performed in a clinical GE 1.5 T MRI scanner (Milwaukee, WI). The control sequences were programmed using the EPIC API. Important parameters of the mechanisms are presented in Table 1.

Three sets of experiments were conducted in order to validate the actuator concept and analysis. In all experiments, slip angle was uncontrolled. The first set of experiments was designed to estimate the viscous and non-viscous friction terms of the model. With these quantities, the performance under closed-loop control of slip angle can be characterized. The second set of experiments demonstrate tissue puncture on a porcine heart and also evaluate the ability to perform MRI tissue imaging in the presence of the actuator. The third and final set of experiments demonstrates an MRI-controlled locking mechanism.

A. MRI experiment 1: Estimation of friction terms

To estimate actuator friction, the actuator was loaded against a set of calibrated MR-compatible springs fabricated using NiTi wire. The springs were calibrated using standard weights. The four springs were housed in a Lego assembly as shown in Fig. 7. The spring assembly and the actuator were mounted on a common Plexiglas base and placed at the isocenter of the scanner. Experiments were performed at four Hz, and different gradient frequencies $\omega = \{1.25, 1.45, 1.6, 2\}$ the blocking force was computed from the maximum spring deflection as the actuator followed a trajectory comparable to that of Fig. 5.

The results of the four measurements are plotted in Fig. 8. The linear interpolation model is given by:

$$F_l = -0.4\omega + 1.3 \tag{28}$$

Comparing (28) to (26c) for slip angle $s = \pi/2$ rad (blocking force condition), the parameters of viscous friction and non-viscous friction are estimated to be:

$$B = 1.3 \cdot 10^{-5} \, \mathrm{Nsm}^{-1}, \, T_{fr} = 2.3 \cdot 10^{-5} \, \mathrm{mN} \tag{29}$$

Now that all parameter values are known, (13) is used to plot in Fig. 9 the relationship between output force F_l and gradient frequency ω, for three different values of B_{grad}. Fig. 10 plots output power versus output linear speed. Note the similarity between these plots and those of DC motors.

B. MRI experiment 2: Porcine heart puncture

This experiment demonstrates an interventional application of the prototype actuator. For these trials, a 21-gauge bevel-tip biopsy needle was attached to the tip of the rack and a swine heart was placed adjacent to the needle tip. Both the heart and the actuator were secured to a Plexiglas base as shown in Fig. 11 and located at the isocenter. Gradient field strengths of 20mT/m and 40mT/m were applied with a rotational frequency of 1Hz.

At 20mT/m, the needle failed to puncture the tough, elastic epicardial layer of the heart. At 40mT/m, the needle successfully punctured the epicardial layer and continued to penetrate the softer underlying myocardium to a depth of approximately 15mm. At this point, the actuator was commanded to reverse direction and was successfully withdrawn from the heart. These results are in agreement with the plots of Fig. 9 since it is known that the maximum epicardial puncture forces for swine hearts at a velocity of 1mm/s, lie in the range of 0.5N to 0.9N [18]. According to Fig. 9, these force requirements are provided by the 40 mT/m input, but not by the 20 mT/m. This experiment appears as an attached video file.

To evaluate the effect of the actuator on tissue imaging, standard imaging sequences were employed to image the biopsy needle inside the heart. While not depicted, it was determined that the SNR signal in the region of interest was unaffected by the ferromagnetic material of the actuator.

C. MRI experiment 3: Locking mechanism

Most robotic applications involve controlling multiple degrees of freedom. In addition, it is important to ensure that the actuators are not accidentally activated during MR imaging and when moving the system in and out of the MR bore. One approach to addressing both issues is to incorporate a locking mechanism into each actuator that is also MR controlled.

As a simple example of this approach, Fig. 12 depicts a locking mechanism consisting of a bar that pivots about its center of mass. The bar contains a ferrous steel sphere at one end and a nonferrous steel sphere at the other end. Consequently, small gradients along the *Y*-axis (e.g. 20mT/m) can be used to rotate the bar between its locked and unlocked configurations. In the locked configuration, the locking bar prevents the actuator lever from rotating.

VI. Conclusions

This paper presents a novel actuator technology for robotically-assisted MR-guided interventions. The actuator is both powered and controlled by the magnetic fields of the MR

scanner. Since the ferromagnetic material of the actuator is small in volume and can be located outside the imaging region of interest, it does not affect image SNR at imaging region.

As demonstrated by analysis and experiments in a clinical 1.5 T scanner, the prototype actuator, constructed from Legos, was capable of generating sufficient force to puncture epicardial tissue. In addition, an MR-powered actuator locking mechanism was demonstrated.

A variety of techniques can be employed to improve the performance characteristics of the actuator. These include the use of low-friction materials for the transmission and bearing surfaces. In addition, the rotor design can be modified to incorporate multiple ferromagnetic spheres and so achieve higher output forces or torques. Furthermore, control of multiple degrees of freedom can be implemented by taking full advantage of the three independent coordinate-direction gradient inputs in combination with more sophisticated locking mechanism designs.

Acknowledgments

References

1. Tsekos, Nikolaos V.; Khanicheh, Azadeh; Christoforou, Eftychios; Mavroidis, Constantinos. Magnetic Resonance–Compatible Robotic and Mechatronics Systems for Image-Guided Interventions and Rehabilitation: A Review Study. Annual Review of Biomedical Engineering. 2007; 9:351–387.

2. Chinzei K, Hata N, Jolesz FA, Kikinis R. MR Compatible Surgical Assist Robot: System Integration and Preliminary Feasibility Study. Int Conf Med Image Comput Comput Assist Interv. 2000; 3:921–930.

3. Masamune K, Kobayashi E, Masutani Y, Suzuki M, Dohi T, et al. Development of an MRI-compatible needle insertion manipulator for stereotactic neurosurgery. J Image Guid Surg. 1995; 1:242–48. [PubMed: 9079451]

4. Hata, N.; Hashimoto, R.; Tokuda, J.; Morikawa, S. Needle guiding robot for MR-guided microwave thermotherapy of liver tumor using motorized remote center-of-motion constraint. Proc. IEEE Int. Conf. Robotics Automation (ICRA); 2005; Barcelona, Spain. p. 1664-68.

5. Tsekos NV, Ozcan A, Christoforou E. A prototype manipulator for MR-guided interventions inside standard cylindrical MRI scanners. J Biomech Eng. 2005; 127:972–80. [PubMed: 16438235]

6. Fischer GS, Krieger A, Iordachita I, Csoma C, Whitcomb LL, Gabor F. MRI compatibility of robot actuation techniques: a comparative study. Med Image Comput Comput Assist Interv. 2008; 11:509–17. [PubMed: 18982643]

7. Kapoor, A.; Wood, B.; Mazilu, D.; Horvath, KA.; Li, Ming. MRI-compatible hands-on cooperative control of a pneumatically actuated robot. Proc. IEEE Int. Conf. Robotics and Automation (ICRA); 12–17 May 2009; p. 2681-2686.

8. Patriciu A, Petrisor D, Muntener M, Mazilu D, Schar M, Stoianovici D. Automatic Brachytherapy Seed Placement Under MRI Guidance. IEEE Transactions on Biomedical Engineering. Aug; 2007 54(8):1499–1506. [PubMed: 17694871]

9. Song, Sang-Eun; Cho, NB.; Fischer, G.; Hata, N.; Tempany, C.; Fichtinger, G.; Iordachita, I. Development of a Pneumatic Robot for MRI-guided Transperineal Prostate Biopsy and Brachytherapy: New approaches. Proc. IEEE Conf. Robotics and Automation (ICRA); 2010; Anchorage, Alaska USA. p. 2580-2585.

10. Martel S, Felfoul O, Mathieu J-B, Chanu A, Tamaz S, Mohammadi M, Mankiewicz M, Tabatabaei N. MRI-based nanorobotic platform for the control of magnetic nanoparticles and flagellated

bacteria for target interventions in human capillaries. International Journal of Robotics Research (IJRR), Special Issue on Medical Robotics. Aug; 2009 28(9):1169–1182.

11. Martel S, Mathieu J-B, Felfoul O, Chanu A, Aboussouan É, Tamaz S, Pouponneau P, Beaudoin G, Soulez G, Yahia L'H, Mankiewicz M. Automatic navigation of an untethered device in the artery of a living animal using a conventional clinical magnetic resonance imaging system. Applied Physics Letters. March 12.2007 90(11):114105. (3 pages).

12. Arcese, L.; Fruchard, M.; Ferreira, A. Nonlinear modeling and robust controller-observer for a magnetic microrobot in a fluidic environment using MRI gradients. Proceedings of the 2009 IEEE/RSJ international conference on Intelligent robots and Systems (IROS); St. Louis, Missouri, USA. p. 534-539.

13. Abbott JJ, Ergeneman O, Kummer MP, Hirt AM, Nelson BJ. Modeling Magnetic Torque and Force for Controlled Manipulation of Soft-Magnetic Bodies. IEEE Transactions on Robotics. Dec; 2007 23(6):1247–1252.

14. Jin, Jianming. Electromagnetic Analysis and Design in Magnetic Resonance Imaging. CRC Press; Boca Raton, FL: 1999.

15. Han BH, Park S, Lee SY. Gradient waveform synthesis for magnetic propulsion using MRI gradient coils. Physics in Medicine and Biology. 53(17):4639. [PubMed: 18695296]

16. http://www.gobearings.com/materials.htm

17. Giffin, A.; Shneider, M.; Chiranjeev, KS.; Ames, TL.; Miles, RB. Effects of a Conducting Sphere Moving Through a Gradient Magnetic Field. AIAA Aerospace Sciences Meeting; Orlando, Florida. Jan 4–7, 2010;

18. Mahvash M, Dupont P. Mechanics of Dynamic Needle Insertion into a Biological Material. IEEE Transactions of Biomedical Engineering. April; 2010 57(4):934–43.
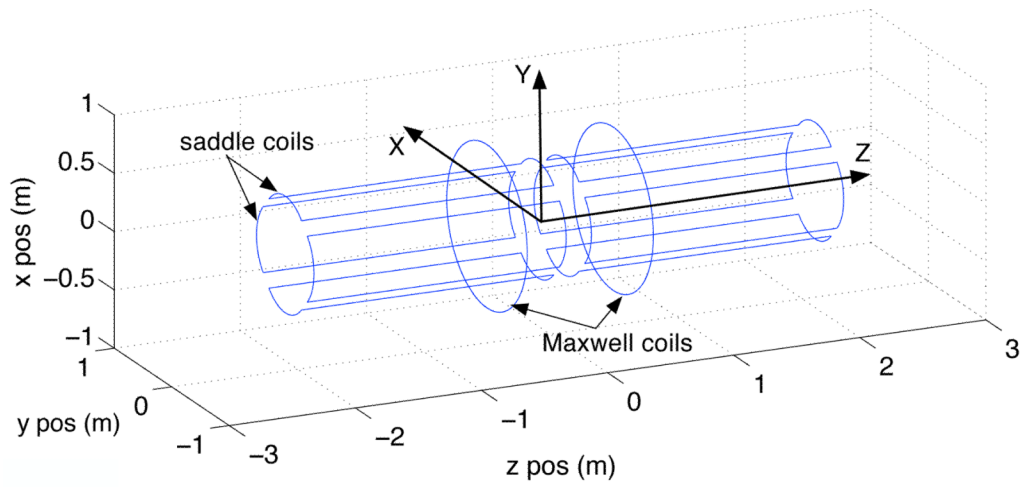
Fig. 1.
MRI gradient coils configuration.
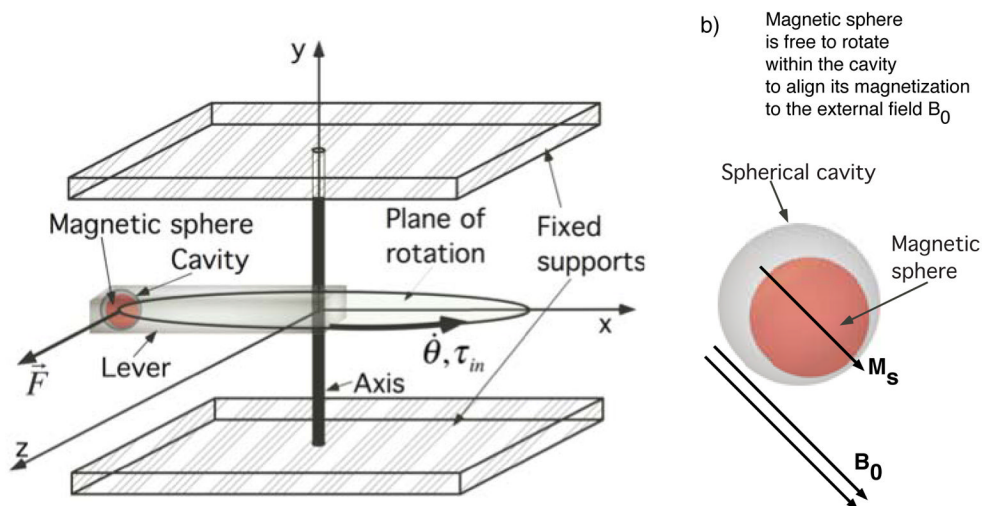
Fig. 2.
Actuator schematic. (a) Complete assembly. (b) Detail of spherical cavity and encapsulated magnetic sphere aligned to the field B_0.
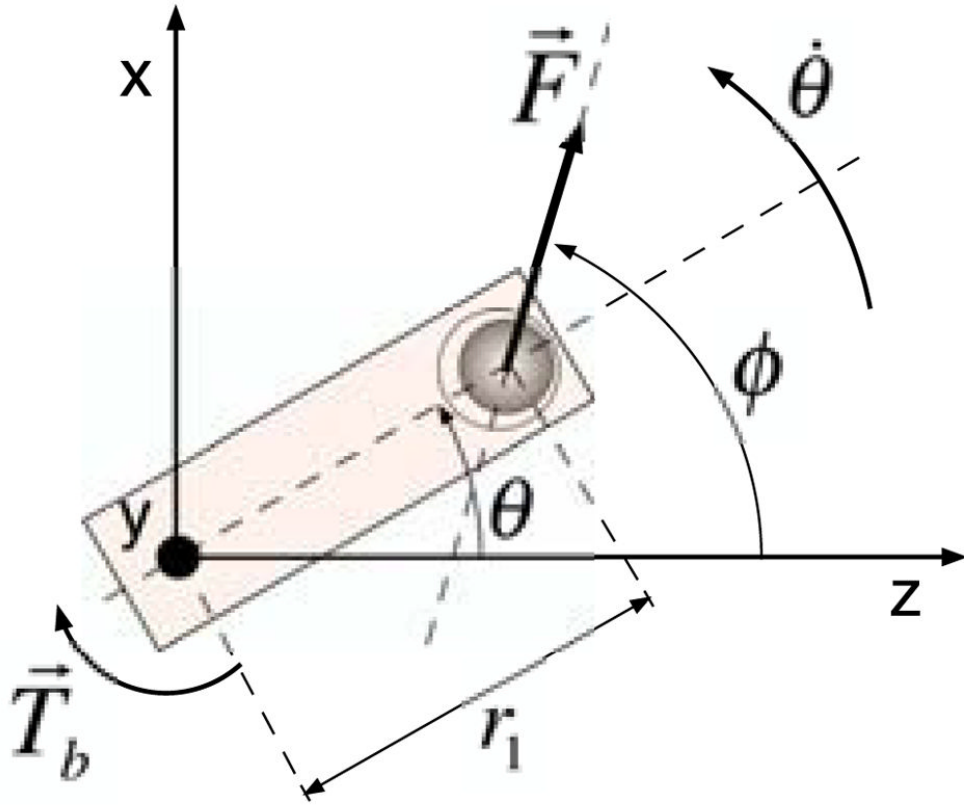
Fig. 3.
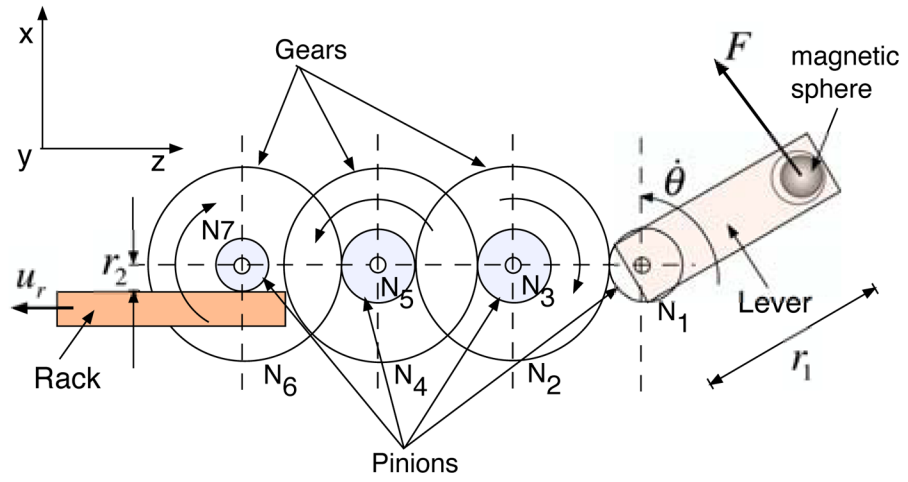Force $\vec{F}$ acts on the sphere and the lever rotates about y-axis.

Fig. 4.
Transmission unit incorporating gear train and rack and pinion elements.
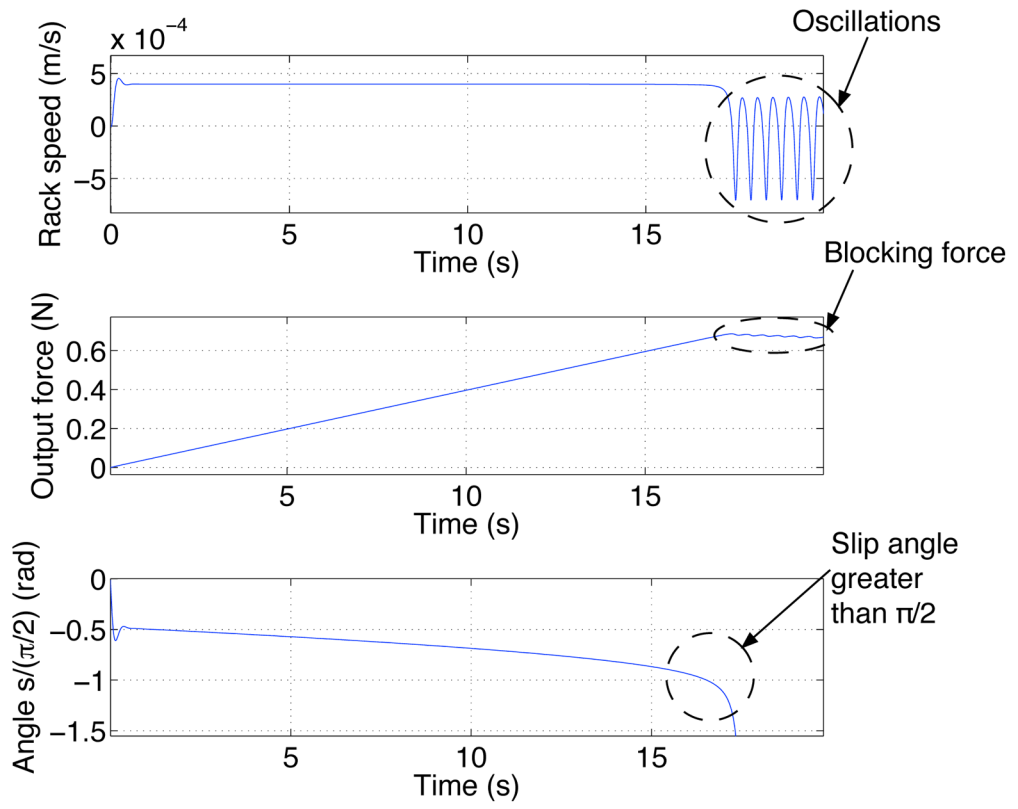
Fig. 5.
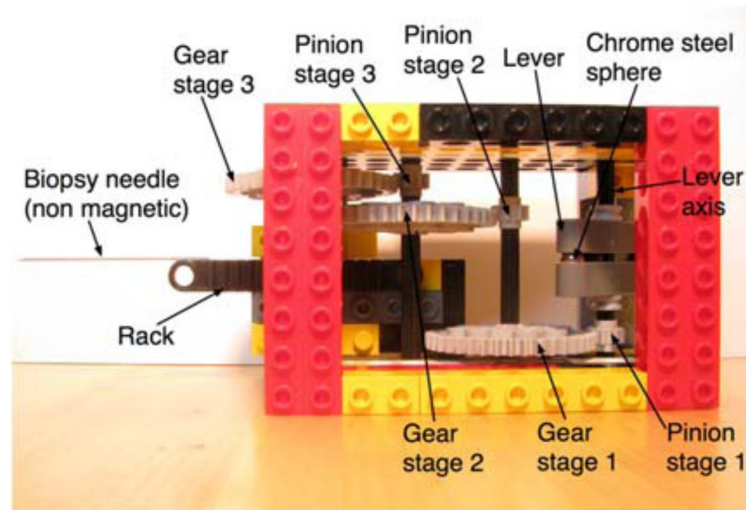Simulation of constant-velocity elastic load response.
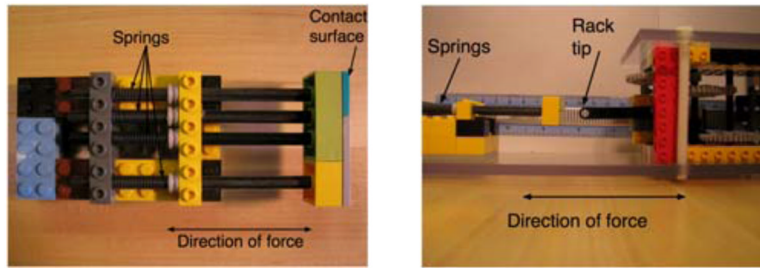
Fig. 6.
Actuator with attached biopsy needle.

Fig. 7.
Fig. 7a. Calibrated spring set for measuring forces applied to contact surface.
Fig. 7b. Actuator rack tip applies forces to contact surface of spring set.
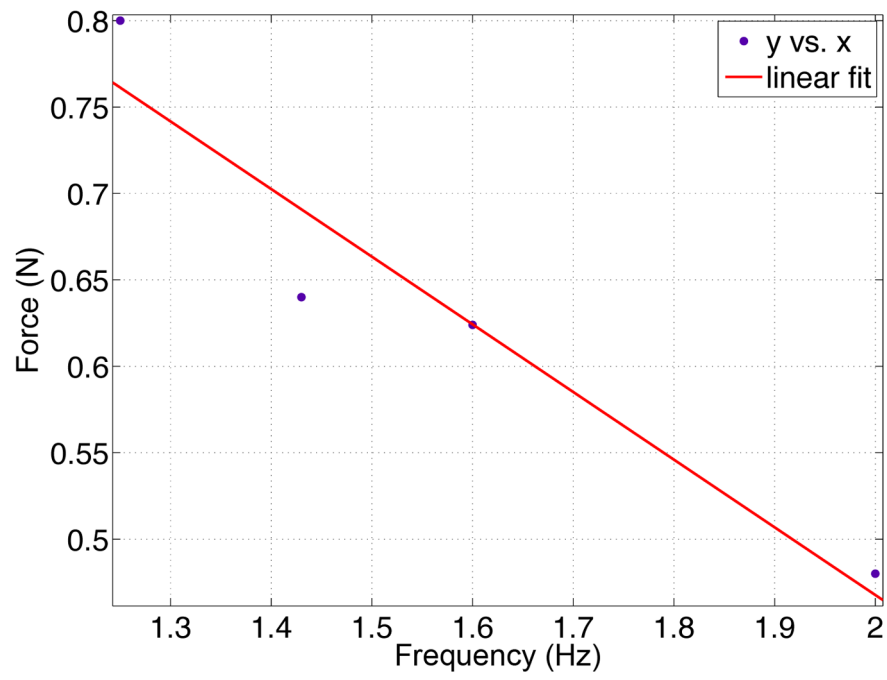
Fig. 8.
Blocking force data and linear fit.
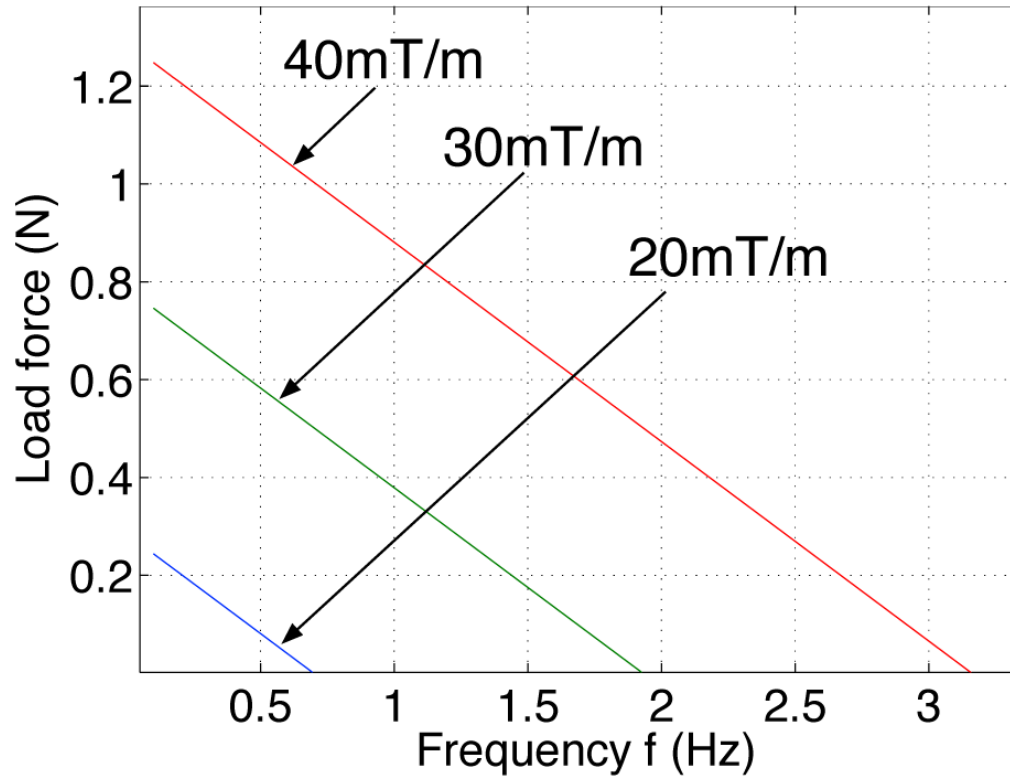
Fig. 9.
Output load versus gradient frequency.
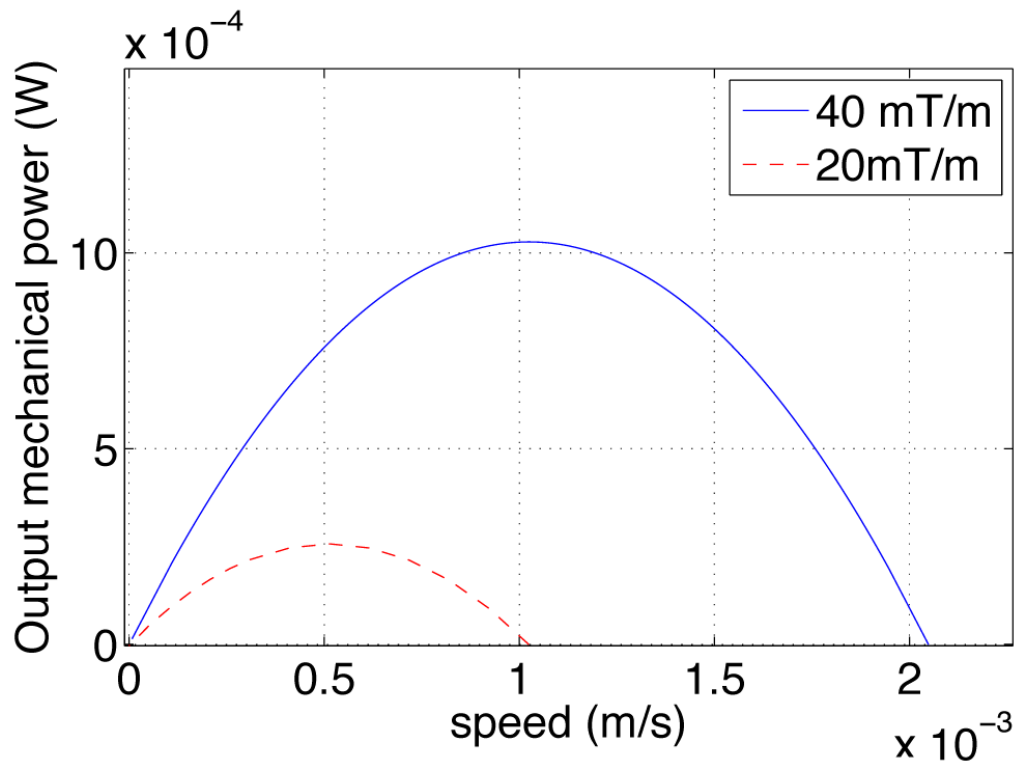
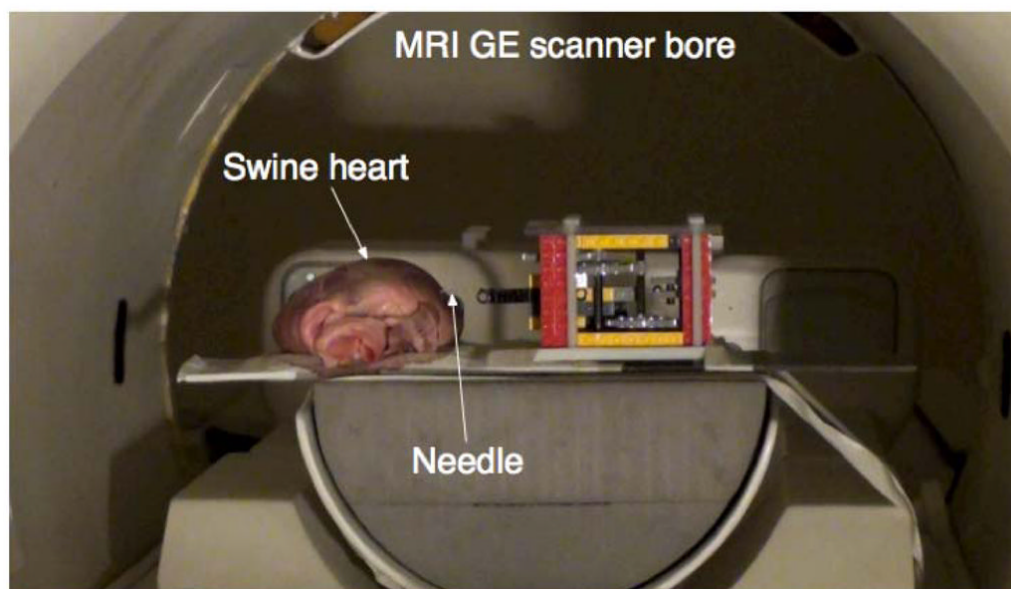**Fig. 10.**
Output mechanical power versus output velocity.

Fig. 11.
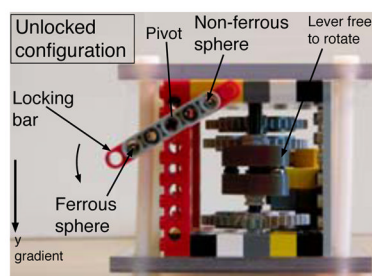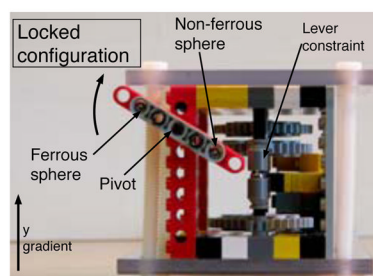Swine heart puncture experiment.

Fig. 12a

Fig. 12b

Fig. 12.
Fig. 12a. Actuator in the unlocked configuration.
Fig. 12b. Actuator in the locked configuration.

Table 1

Actuator Parameters

Parameter	Value
Sphere radius [mm]	2.5
Sphere magnetization [Am^{-1}]	1.36 10^6
Transmission ratio R [−]	3.2 10^{-5}
Moment arm r_1 [mm]	18
Magnetic gradient [mTm^{-1}]	40
Duty cycle of MRI gradient coils [%]	100